J. Fluid Mech. (2006), *vol.* 547, *pp.* 361–388. © 2006 Cambridge University Press
doi:10.1017/S0022112005007317 Printed in the United Kingdom

Numerical study of three-dimensional overturning waves in shallow water

By P. GUYENNE[1] AND S. T. GRILLI[2]

[1]Department of Mathematics, McMaster University, Hamilton, ON L8S4K1, Canada

[2]Department of Ocean Engineering, University of Rhode Island, Narragansett, RI 02882, USA

(Received 20 October 2004 and in revised form 18 July 2005)

Simulations in a three-dimensional numerical wave tank are performed to investigate the shoaling and breaking of solitary waves over a sloping ridge. The numerical model solves fully nonlinear potential flow equations with a high-order boundary-element method combined with an explicit time-integration method, expressed in a mixed Eulerian–Lagrangian formulation. Analyses of shoaling and breaking-wave profiles and kinematics (both on the free surface and within the flow) are carried out. It is observed that the transverse modulation of the ridge topography induces three-dimensional effects on the time evolution, shape and kinematics of breaking waves. Comparisons of two- and three-dimensional results in the middle cross-section of the ridge, however, show remarkable similarities, especially for the shape and dynamics of the plunging jet.

1. Introduction

Over the last two decades, many studies have been carried out to achieve a better understanding of the breaking of surface water waves. For instance, a description of the dynamics of breaking waves is necessary to explain the mechanisms of air–sea interactions, such as energy and momentum transfer from wind to water and from waves to currents, and the generation of turbulence in the upper ocean. In nearshore areas, breaking-wave induced currents are the driving mechanism for sediment transport, which leads to beach erosion and accretion. The study of breaking waves is also of importance in naval and marine engineering applications, owing to their damaging effects on ships and offshore structures in heavy seas. Despite significant progress, the process of wave breaking has not yet been fully explained owing to its complexity. See Peregrine (1983) and Banner & Peregrine (1993) for reviews of wave breaking in shallow and deep water, respectively.

The present paper reports on numerical simulations aimed at describing the early stages of wave breaking induced by changes in topography in shallow water, namely the phenomenon of wave overturning. We concentrate on cases in which the bottom topography induces three-dimensional effects on the flow, and we pay particular attention to plunging breakers which are characterized by the formation of a more prominent jet. A high-order three-dimensional numerical model solving fully nonlinear potential flow equations is used. The potential flow approximation is justified for initially irrotational waves (such as the solitary waves used here as incident waves), considering the slow diffusion of vorticity from boundaries until the breaker jet touches down. In fact, comparisons of two-dimensional numerical results with laboratory experiments have consistently shown that the full potential theory accurately predicts

the characteristics of wave overturning in deep water (e.g. Dommermuth *et al.* 1988; Skyner 1996), as well as wave shoaling and overturning over slopes (e.g. Grilli *et al.* 1994; Grilli, Svendsen & Subramanya 1997).

Most of the numerical studies of wave breaking so far have focused on two-dimensional problems. Significant contributions in the numerical simulation of steep fully nonlinear waves, based on potential flow theory, were made by Longuet-Higgins & Cokelet (1976) who developed a mixed Eulerian–Lagrangian (MEL) approach combined with a boundary integral equation (BIE) formulation. Their computations were limited to a periodic domain in deep water and they were able to reproduce overturning waves by specifying a localized surface pressure. Similar methods were adopted in subsequent works, for example, by Vinje & Brevig (1981) and Baker, Meiron & Orszag (1982) who considered the case of finite depth. Results obtained by New, McIver & Peregrine (1985), for plunging waves over constant depth, greatly contributed to our understanding of breaking wave kinematics. They carried out high-resolution computations for various types of breakers and analysed in detail the overturning motions by following fluid particle trajectories in the space, velocity and acceleration planes. More recent two-dimensional models can accommodate both arbitrary waves and complex bottom topography. They are directly implemented in a physical space region where incident waves can be generated at one extremity and reflected, absorbed or radiated at the other extremity (e.g. Cointe 1990; Grilli & Subramanya 1996; Grilli & Horrillo 1997). For these reasons, they are often referred to as numerical wave tanks (NWT).

Only a few attempts, however, have been made to extend the numerical simulations to three dimensions, owing to the more difficult geometric representation and the limitations of computer power (e.g. Boo, Kim & Kim 1994; Ferrant 1996; Celebi, Kim & Beck 1998; Clamond *et al.* 2005; Fructus *et al.* 2005). In particular, the problem of strongly nonlinear waves requires very accurate and stable numerical methods, and this consequently leads to an increase of the computational cost. Xü & Yue (1992) and Xue *et al.* (2001) calculated three-dimensional overturning waves in a doubly periodic domain with infinite depth (i.e. only the free surface is discretized). They used a high-order quadratic boundary-element method (BEM) to solve the equations in an MEL formulation. As in Longuet-Higgins & Cokelet (1976), the initial conditions were progressive Stokes waves and a localized surface pressure was applied to make waves break. These authors performed a detailed analysis of the kinematics of plunging waves and quantified the three-dimensional effects on the flow. Broeze (1993) and Broeze, Van Daalen & Zandbergen (1993) developed a similar method for a non-periodic domain with finite depth. They were also able to produce the initial stages of wave overturning over a bottom obstacle.

Grilli, Guyenne & Dias (2001) proposed an accurate three-dimensional NWT for the description of strongly nonlinear waves over complex bottom topography. This NWT is based on an MEL explicit time stepping and a high-order BEM with third-order spatial discretization, ensuring local continuity of the inter-element slopes. Arbitrary waves can be generated in this NWT and, if required, absorbing conditions can be specified on lateral boundaries. Although an application to the shoaling of a solitary wave up to overturning was shown, these authors focused more on the derivation and validation of their numerical model and methods rather than on the physical implications of results. Other applications of this NWT to nonlinear wave processes can be found in Guyenne, Grilli & Dias (2000) for the modelling of wave impact on a vertical wall, in Brandini & Grilli (2001*a*, *b*) for the modelling of freak wave generation due to directional wave focusing, and in Grilli, Vogelmann &

Watts (2002) for the modelling of tsunami generation by submarine mass failure. For further information on boundary-integral methods, especially in applications to three-dimensional free-surface flows, see Tong (1997).

In the present paper, the breaking of solitary waves over a sloping ridge is investigated in more detail using the model of Grilli *et al.* (2001), with some recent improvements and extensions. The initial solitary wave is a numerically exact solution computed by Tanaka's method (see Tanaka 1986). Because of the complexity of the problem and the high computational cost, our study of three-dimensional breakers is restricted to a limited number of configurations of the bottom geometry, domain size and incident wave height. New results are obtained for the velocity and acceleration fields during wave overturning, both on the free surface and within the flow. As before, no smoothing of the solution is required to suppress spurious waves at any time in the computations. Since we consider the three-dimensional problem in shallow water and wave breaking induced by topographical effects, our numerical study can be viewed as complementary to that of Xue *et al.* (2001).

The paper is organized as follows. In § 2, we review the mathematical formulation of the wave model. The derivation and method of computation of the internal velocity and acceleration fields are also presented. We review the numerical methods for temporal and spatial discretizations in § 3 and indicate where these have been improved as compared to earlier formulations of the model. Finally, cases of solitary waves propagating and overturning over a sloping ridge are analysed in § 4.

2. Mathematical formulation

Equations for a fully nonlinear potential flow with a free surface are listed below. The velocity potential $\phi(\boldsymbol{x}, t)$ is introduced to describe an inviscid irrotational flow in Cartesian coordinates $\boldsymbol{x} = (x, y, z)$ with z the vertical upward direction ($z = 0$ at the undisturbed free surface), and the fluid velocity is expressed as $\boldsymbol{u} = \nabla\phi$.

The continuity equation in the fluid domain $\Omega(t)$ with boundary $\Gamma(t)$ is Laplace's equation

$$\nabla^2\phi = 0. \tag{2.1}$$

The corresponding three-dimensional free-space Green's function is defined as

$$G(\boldsymbol{x}, \boldsymbol{x}_l) = \frac{1}{4\pi r} \quad \text{with} \quad \frac{\partial G}{\partial n}(\boldsymbol{x}, \boldsymbol{x}_l) = -\frac{1}{4\pi}\,\frac{\boldsymbol{r}\cdot\boldsymbol{n}}{r^3}, \tag{2.2}$$

where $r = |\boldsymbol{r}| = |\boldsymbol{x} - \boldsymbol{x}_l|$ is the distance from the source point $\boldsymbol{x}$ to the field point $\boldsymbol{x}_l$ (both on boundary Γ), and $\boldsymbol{n}$ is the outward unit vector normal to the boundary at point $\boldsymbol{x}$.

Green's second identity transforms (2.1) into the BIE

$$\alpha(\boldsymbol{x}_l)\phi(\boldsymbol{x}_l) = \int_\Gamma \left[\frac{\partial\phi}{\partial n}(\boldsymbol{x})G(\boldsymbol{x}, \boldsymbol{x}_l) - \phi(\boldsymbol{x})\frac{\partial G}{\partial n}(\boldsymbol{x}, \boldsymbol{x}_l)\right] \mathrm{d}\Gamma, \tag{2.3}$$

where $\alpha(\boldsymbol{x}_l) = (1/4\pi)\theta_l$ and θ_l is the exterior solid angle at point $\boldsymbol{x}_l$.

The boundary is divided into various parts satisfying different boundary conditions (figure 1). On the free surface $\Gamma_f(t)$, ϕ satisfies the nonlinear kinematic and dynamic boundary conditions in the MEL formulation,

$$\frac{\mathrm{D}\boldsymbol{R}}{\mathrm{D}t} = \boldsymbol{u} = \nabla\phi, \tag{2.4}$$

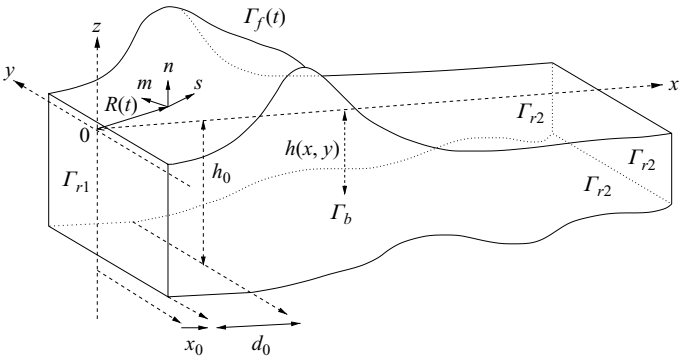

FIGURE 1. Sketch of the computational domain for the three-dimensional NWT.

$$\frac{\mathrm{D}\phi}{\mathrm{D}t} = -gz + \tfrac{1}{2}\nabla\phi\cdot\nabla\phi - \frac{p}{\rho}, \tag{2.5}$$

respectively, with $\boldsymbol{R}$ being the position vector of a fluid particle on the free surface, g the acceleration due to gravity, p the atmospheric pressure, ρ the fluid density and $\mathrm{D}/\mathrm{D}t = \partial/\partial t + \nabla\phi\cdot\nabla$ the Lagrangian time derivative. The effects of surface tension are neglected.

Incident waves can be generated in the NWT by simulating a wavemaker at the 'open sea' boundary Γ_{r1} (Brandini & Grilli 2001*a*, *b*). Here, however, we directly specify the incident wave at $t = 0$. On the bottom Γ_b and other fixed parts of the boundary referred to as Γ_{r2}, a no-flow condition is prescribed as

$$\frac{\partial\phi}{\partial n} = 0. \tag{2.6}$$

Once the BIE (2.3) is solved, the solution within the domain can be evaluated from the boundary values. Using (2.3), the internal velocity is given by

$$\boldsymbol{u}(\boldsymbol{x}_l) = \nabla\phi(\boldsymbol{x}_l) = \int_\Gamma \left[\frac{\partial\phi}{\partial n}(\boldsymbol{x})\,\boldsymbol{Q}(\boldsymbol{x},\boldsymbol{x}_l) - \phi(\boldsymbol{x})\frac{\partial\boldsymbol{Q}}{\partial n}(\boldsymbol{x},\boldsymbol{x}_l)\right]\mathrm{d}\Gamma, \tag{2.7}$$

with

$$\boldsymbol{Q}(\boldsymbol{x},\boldsymbol{x}_l) = \frac{1}{4\pi r^3}\boldsymbol{r}, \quad \frac{\partial\boldsymbol{Q}}{\partial n}(\boldsymbol{x},\boldsymbol{x}_l) = \frac{1}{4\pi r^3}\left[\boldsymbol{n} - 3(\boldsymbol{r}\cdot\boldsymbol{n})\frac{\boldsymbol{r}}{r^2}\right], \tag{2.8}$$

and r denoting the distance from the boundary point $\boldsymbol{x}$ to the interior point $\boldsymbol{x}_l$. Note that the coefficient $\alpha(\boldsymbol{x}_l)$ reduces to unity for interior points.

Similarly, we can also derive the internal Lagrangian acceleration

$$\frac{\mathrm{D}\boldsymbol{u}}{\mathrm{D}t} = \frac{\mathrm{D}}{\mathrm{D}t}\nabla\phi = \frac{\partial}{\partial t}\nabla\phi + (\nabla\phi\cdot\nabla)\nabla\phi, \tag{2.9}$$

where the first term on the right-hand side, corresponding to the local acceleration, is given by

$$\nabla\frac{\partial\phi}{\partial t}(\boldsymbol{x}_l) = \int_\Gamma \left[\frac{\partial^2\phi}{\partial t\,\partial n}(\boldsymbol{x})\,\boldsymbol{Q}(\boldsymbol{x},\boldsymbol{x}_l) - \frac{\partial\phi}{\partial t}(\boldsymbol{x})\frac{\partial\boldsymbol{Q}}{\partial n}(\boldsymbol{x},\boldsymbol{x}_l)\right]\mathrm{d}\Gamma, \tag{2.10}$$

and the last term is computed using (2.7) and differentiating $\nabla\phi$. This requires calculating the spatial derivatives for all components of $\boldsymbol{Q}$ and $\partial\boldsymbol{Q}/\partial n$. Their

expressions are

$$\frac{\partial Q_i}{\partial x_j} = \begin{cases} \dfrac{3}{4\pi r^5} r_i r_j, & i \neq j \\ \dfrac{1}{4\pi r^3}\left(\dfrac{3}{r^2} r_i^2 - 1\right), & i = j, \end{cases} \tag{2.11}$$

$$\frac{\partial}{\partial x_j}\left(\frac{\partial Q_i}{\partial n}\right) = \begin{cases} \dfrac{3}{4\pi r^5}\left[r_j n_i + r_i n_j - \dfrac{5}{r^2}(\boldsymbol{r}\cdot\boldsymbol{n}) r_i r_j\right], & i \neq j \\ \dfrac{3}{4\pi r^5}\left[\boldsymbol{r}\cdot\boldsymbol{n} + 2 r_i n_i - \dfrac{5}{r^2}(\boldsymbol{r}\cdot\boldsymbol{n}) r_i^2\right], & i = j, \end{cases} \tag{2.12}$$

where i, j refer to the spatial dimensions and r_i stands for the ith component of $\boldsymbol{r}$.

The quantities $\partial\phi/\partial t$ and $\partial^2\phi/\partial t\partial n$ in (2.10) also satisfy a BIE similar to (2.3) for ϕ and $\partial\phi/\partial n$. In fact, the calculation of their values on the free surface is done as part of the second-order time-integration method outlined in § 3.1. Note that the results presented here are restricted to a no-flow condition on all lateral boundaries Γ_{r1} and Γ_{r2}. For the use of 'snake' flap wavemaker and absorbing piston boundaries at extremities of the NWT, see Brandini & Grilli (2001*a, b*) and Grilli *et al.* (2002).

3. Numerical methods

Details of the implementation and performance of the three-dimensional NWT are given in Grilli *et al.* (2001). We only summarize here the methods for temporal and spatial discretizations and indicate some recent improvements.

3.1. *Time integration*

A second-order explicit scheme based on Taylor series expansions is used to update the position $\boldsymbol{R}$ and velocity potential ϕ on the free surface, as

$$\boldsymbol{R}(t + \Delta t) = \boldsymbol{R} + \Delta t \frac{\mathrm{D}\boldsymbol{R}}{\mathrm{D}t} + \frac{\Delta t^2}{2}\frac{\mathrm{D}^2\boldsymbol{R}}{\mathrm{D}t^2} + O(\Delta t^3), \tag{3.1}$$

$$\phi(t + \Delta t) = \phi + \Delta t \frac{\mathrm{D}\phi}{\mathrm{D}t} + \frac{\Delta t^2}{2}\frac{\mathrm{D}^2\phi}{\mathrm{D}t^2} + O(\Delta t^3), \tag{3.2}$$

where Δt is the varying time step and all terms in the right-hand sides are evaluated at time t.

First-order coefficients in these Taylor series are given by (2.4) and (2.5), which requires the calculation of ϕ, $\partial\phi/\partial n$ at time t on the free surface. Second-order coefficients are obtained from the Lagrangian time derivative of (2.4) and (2.5), which also requires the calculation of $\partial\phi/\partial t$, $\partial^2\phi/\partial t\partial n$ at time t. Since the BIEs to be solved in both cases correspond to the same boundary geometry, we must discretize and assemble the resulting linear system only once. Other advantages of this time-stepping scheme are of being explicit and using spatial derivatives of the field variables in the evaluation of values at $t + \Delta t$, which provides a good stability of the computed solution.

The time step Δt in (3.1) and (3.2) is adaptively selected at each time as

$$\Delta t = C_0 \frac{\Delta r^{min}}{\sqrt{gh}}, \tag{3.3}$$

where C_0 denotes the Courant number, $\Delta r^{\min}$ is the instantaneous minimum distance between two neighbouring nodes on Γ_f and h is a characteristic depth.

Global accuracy of the numerical scheme can be assessed at any time by checking the conservation of volume

$$V = \int_\Gamma z n_z \, \mathrm{d}\Gamma, \tag{3.4}$$

and total energy

$$E = \tfrac{1}{2}\rho \int_\Gamma \left(\phi \frac{\partial \phi}{\partial n} + g z^2 n_z \right) \mathrm{d}\Gamma, \tag{3.5}$$

where the first and second terms represent the kinetic and potential contributions of the flow, respectively, and n_z is the vertical component of the unit normal vector.

Grilli *et al.* (2001) found that the errors on volume and energy conservation reach a minimum for $C_0 \simeq 0.45$. This implies, in particular, that Δt could not be imposed too small, otherwise numerical errors would accumulate faster when solving the BIEs at intermediate times. It is emphasized that no smoothing/filtering was used to stabilize the solution in all cases we considered.

3.2. *Boundary discretization*

A high-order three-dimensional BEM is used to solve numerically the BIEs for ϕ and $\partial\phi/\partial t$. The boundary is discretized into collocation nodes, defining two-dimensional elements for local interpolations of the solution in between these nodes. Thus, within each element, the boundary geometry and field variables are interpolated using polynomial shape functions. Generally, isoparametric elements can provide a high-order approximation within their area of definition, but only offer $\mathscr{C}^0$ continuity of the geometry and field variables at nodes in between elements. A robust treatment requires definition of elements which are both high-order within their area of definition and at least locally $\mathscr{C}^2$ continuous at their edges. For this purpose, an extension of the so-called middle-interval-interpolation method introduced by Grilli & Subramanya (1996) has been developed in the three-dimensional model. The boundary elements are 4×4-node quadrilaterals associated with bi-cubic shape functions. Only one out of the nine sub-quadrilaterals so defined is used for the interpolation, depending on the location of the element with respect to the edges of the NWT.

Double and triples nodes are introduced to specify the BIEs at intersections of the boundary (i.e. at edges and corners of the NWT). This makes the model especially suitable for problems involving wave–body interactions. The discretized boundary integrals are evaluated for each collocation node by numerical integration. When the collocation node does not belong to the integrated element, a standard Gauss–Legendre quadrature is applied. When it belongs to the element, the distance r in the Green's function and in its normal gradient vanishes at one of the nodes of the element. For such singular situations, a method of singularity extraction is used based on polar coordinate transformations. Tangential derivatives in (3.1) and (3.2) are calculated by defining fourth-order 5×5-node elements (Grilli *et al.* 2001). Fochesato, Grilli & Guyenne (2005) proposed more accurate and general expressions of these derivatives, which are used in the present applications.

The linear algebraic system resulting from the discretization of the BIE (2.3) for ϕ (and $\partial\phi/\partial t$) is in general dense and non-symmetric. Since the total number of nodes N_Γ can be very large in three dimensions, the solution by a direct method of order N_Γ^3 is prohibitive. As in Xü & Yue (1992) and Xue *et al.* (2001), a generalized minimal residual (GMRES) algorithm with preconditioning is used to solve the linear system iteratively.

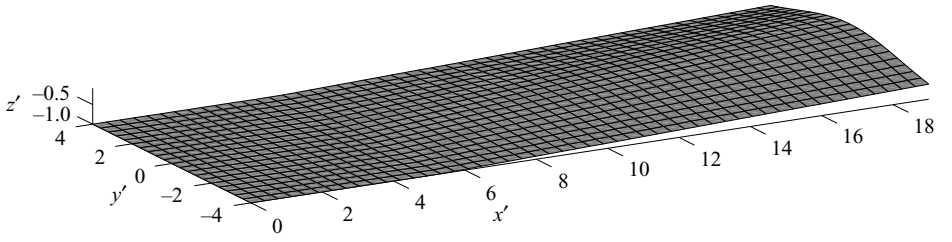

FIGURE 2. Bottom topography and its initial discretization for the shoaling of a solitary wave, modelled as a ridge with a 1:15 slope in the x-direction and a lateral $\mathrm{sech}^2(ky')$ modulation. The configuration $k = 0.25$ is represented here.

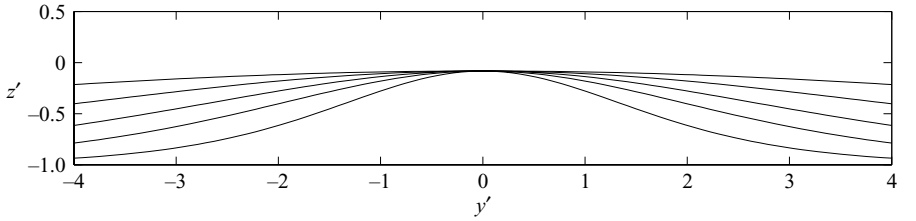

FIGURE 3. Transverse variations of the bottom topography as $\mathrm{sech}^2(ky')$ for $k = 0.1$, 0.17, 0.25, 0.34, 0.5 (from moderately to rapidly decaying transverse tails, respectively).

4. Numerical results

In this section, the numerical model described above is used to compute the shoaling and breaking of solitary waves over a sloping ridge. We present results on the three-dimensional evolution of wave profiles and kinematics (both on the free surface and within the flow). Three-dimensional effects on wave breaking are examined by varying the transverse geometry of the bottom ridge. Comparisons between two- and three-dimensional wave breaking are performed. We also examine the sensitivity of computations to domain size, and perform computations for varying incident wave heights.

4.1. *Solitary wave breaking over a sloping ridge: dependence on bottom variations*

In reviewing the literature, we found that various methods were used for inducing wave breaking in numerical simulations, depending on the physical situation to be simulated. For instance, a localized surface pressure was applied over water of infinite or constant depth to increase wave energy gradually, as happens under wind action, or an initial periodic wave was specified with a sufficiently large (usually non-physical) amplitude so that the computation always rapidly evolves towards breaking. Here, for shallow water-wave transformations, breaking occurs as a result of shoaling over a non-uniform bottom topography, as it is typically the case for breaking waves on beaches.

More specifically, for the purpose of inducing three-dimensional breaking, we specify a somewhat idealized sloping bottom topography in our NWT. As shown in figure 2, the water depth is constant in the first part of the tank ($z = -h_0$). A sloping ridge starts at $x' = 5.225$, with a 1:15 slope in the middle cross-section and a transverse modulation of the form $\mathrm{sech}^2(ky')$. Primes hereinafter indicate non-dimensional variables based on long-wave theory, i.e. lengths are divided by h_0 and times divided by $\sqrt{h_0/g}$. In computations, we will successively set $k = 0.1, 0.17, 0.25, 0.34, 0.5$, which correspond to different amplitudes for the transverse tails of the ridge (figure 3). Our goal is

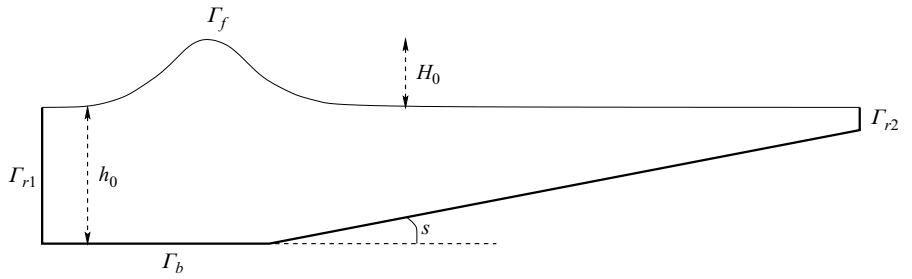

FIGURE 4. Two-dimensional sketch of the experimental set-up. The initial condition is a numerically exact solitary wave of height H_0. It is computed by Tanaka's method and is initially specified in the region of constant depth h_0. The vertical scale is exaggerated.

to examine three-dimensional depth-induced effects on the dynamics and kinematics of breaking waves. Note that, in this paper, we will restrict ourselves to sloping bottom geometries because they represent a good compromise between geometric complexity and computational effort. As shown below, the three-dimensional wave breaking occurring in such configurations already exhibits significant differences in time evolution and wave profiles as compared to the typical two-dimensional wave breaking over a plane slope.

The computational domain is of width $8h_0$ in the y-direction and is truncated at $x' = 19$ in the x-direction, with minimum depth $z' = -0.082$ in the middle ($y' = 0$). Note, this truncation is introduced to reduce the size of the domain, and hence computational cost, since wave overturning always occurs in deeper water for the specified incident waves and bottom topography. We verified that this does not influence results significantly in the overturning region of the wave, by comparing results for different truncations or no truncation at all. The initial condition is a two-dimensional fully nonlinear solitary wave of height $H_0' = 0.6$ and speed $c_0' = 1.25$ with the crest located at $x_0' = 5.785$ for $t' = 0$ (figure 4). This corresponds to a numerically exact solution of potential flow theory computed by Tanaka's (1986) method. Such a wave should propagate without change of shape and speed on uniform depth in our NWT (Grilli *et al.* 2001). The height of the incident solitary wave is chosen large enough for breaking to occur early in the computations, which saves computational time. In practice, this could correspond to the situation where the wave has already propagated quite a long distance from offshore. The imposed (maximum) slope of the bottom is also fairly steep in order to generate a plunging breaker, as it is well known that the type of breaking depends on beach slope in shallow water (e.g. Grilli *et al.* 1997). Note that the choice of solitary waves is motivated by their intrinsic relevance as a good approximation of both tsunamis and long nearshore waves.

The initial discretization for the bottom and free surface consists of 50×20 quadrilateral elements in the x- and y-directions respectively ($\Delta x_0' = 0.38$ and $\Delta y_0' = 0.4$). The lateral boundaries have grid lines connecting the edge nodes of the bottom and free surface, with four elements specified in the vertical direction. Consequently, the total number of nodes is $N_\Gamma = 2862$ and the initial time step is set to $\Delta t_0' = 0.171$ for $C_0 = 0.45$. Computations are first performed in this discretization as long as errors remain acceptable (i.e. less than 0.05% or so on wave mass and energy). A two-dimensional regridding to a finer resolution is then applied at a time when the wave profile is still single-valued. The discretization is increased to 60×40 quadrilateral elements in the portion $8 \leqslant x' \leqslant 19$ of the bottom and free

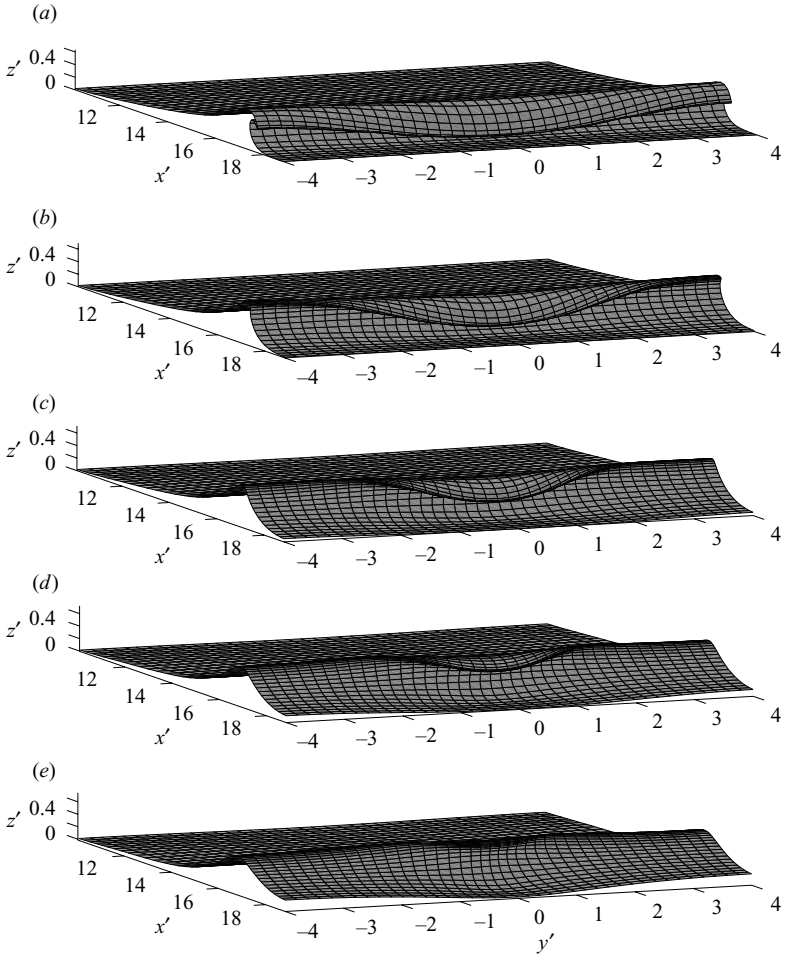

FIGURE 5. Wave profiles for (*a*) $k = 0.1$, (*b*) $k = 0.17$, (*c*) $k = 0.25$, (*d*) $k = 0.34$ and (*e*) $k = 0.5$ at $t' = 8.926$. In all cases, the initial solitary wave is of height $H_0' = 0.6$.

surface ($\Delta x' = 0.18$, $\Delta y' = 0.2$ and $N_\Gamma = 6022$). The procedure consists in regridding over large areas of the discretization at a time when errors are still very small, which guarantees the accuracy of the regridded solution. For instance, regridding was applied at $t' = 4.900$ for $k = 0.25$, when errors on volume and energy conservation are 0.010% and 0.013%, respectively. We chose similar regridding times for the other values of k.

Figure 5 shows the wave profiles for $k = 0.1$, 0.17, 0.25, 0.34, 0.5 at the same time $t' = 8.926$, whereas figure 6 shows the same set of wave profiles in the latest stages of overturning before the computations break down. This typically occurs when two surface nodes propagate too close to each other, in the tip of the plunging jet, and at a time which depends on the selected discretization and numerical parameters. Figure 7 plots the time evolution of numerical errors on the conservation of energy E and volume V, for $k = 0.1$, 0.17, 0.25, 0.34, 0.5, after the regridding times. The reference energy E_0 and volume V_0 are chosen at these times because the computational domain is reduced to $8 \leqslant x' \leqslant 19$ when regridding and so it would not be consistent to compute errors with respect to values at $t' = 0$ for which the domain is larger.

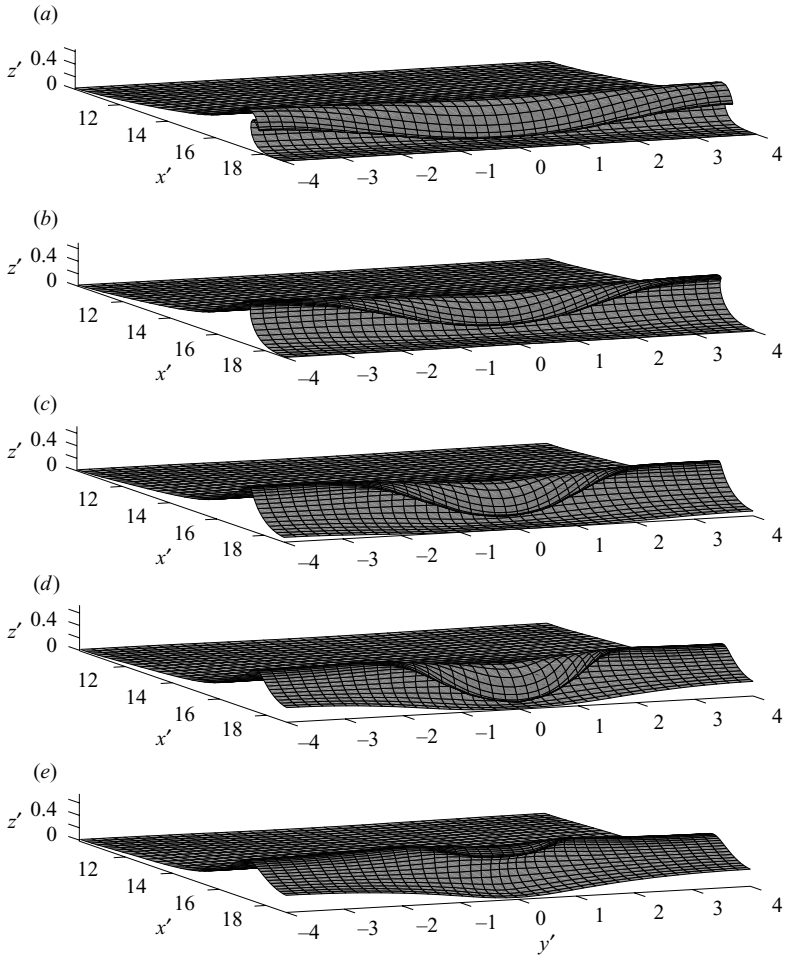

FIGURE 6. Wave profiles for (*a*) $k = 0.1$ ($t' = 8.958$), (*b*) $k = 0.17$ ($t' = 8.926$), (*c*) $k = 0.25$ ($t' = 9.142$), (*d*) $k = 0.34$ ($t' = 9.427$) and (*e*) $k = 0.5$ ($t' = 9.243$).

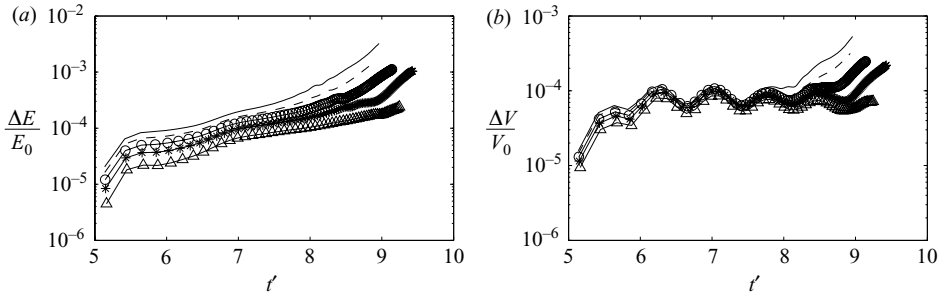

FIGURE 7. Numerical relative errors on the conservation of (*a*) energy E and (*b*) volume V as functions of time, after the instant when the free surface regridding is applied, for $k = 0.1$ (solid line), $k = 0.17$ (dashed line), $k = 0.25$ (solid line, circles), $k = 0.34$ (solid line, stars), $k = 0.5$ (solid line, triangles).

Dimension	s	k	t'_B	x'_B	z'_B	h'_B	z'_B/h'_B
2	0.028	–	11.501	20.457	0.754	0.573	1.316
2	0.052	–	8.570	16.885	0.709	0.389	1.823
2	0.067	–	7.629	15.752	0.680	0.298	2.282
3	0.067	0.10	7.661	15.802	0.685	0.295	2.322
3	0.067	0.17	7.757	15.904	0.693	0.288	2.406
3	0.067	0.25	7.890	16.093	0.706	0.275	2.567
3	0.067	0.34	8.147	16.470	0.719	0.250	2.876
3	0.067	0.50	8.639	17.100	0.740	0.208	3.558

TABLE 1. Bottom slope s, time t'_B, position of maximum surface elevation (x'_B, z'_B), water depth h'_B and breaker height ratio z'_B/h'_B at the breaking point at $y'=0$ for $k=0.1$, 0.17, 0.25, 0.34, 0.5. For comparison, two-dimensional results corresponding to the bottom slopes at $y'=\pm 4$, ± 2, 0 in the three-dimensional case $k=0.25$, are also shown.

In doing so, the numerical errors that we obtain still give a good estimate of the accuracy of our computations since, as mentioned earlier, the solution at the regridding time should be little affected by errors in the initial discretization. In all cases, we see that both types of error remain small up to the latest computed times. For instance, for $k=0.25$, the errors on E and V only reach 0.112% and 0.025%, respectively, at $t'=9.142$.

We see in figure 6 that the larger the value of k, the more localized the breaking process in the middle section (near $y'=0$). In all cases except $k=0.5$, the computations reach an advanced stage of wave overturning characterized by a prominent plunging jet. For $k=0.1$, the bottom exhibits small transverse variations and therefore the resulting wave breaking is almost invariant by translation along the y-axis (figure 6*a*). For a more localized ridge ($k=0.5$), there is a stronger transverse modulation of the wave crest: a much lower crest develops around $y'=0$. In all the configurations, we could have exploited the symmetry of the problem, but this was not done for practical reasons, since our numerical model was developed and implemented for arbitrary bottom topographies. This option might be considered in the future to reduce the computational effort. Nevertheless, it is comforting to see that the solution remains symmetric about the centre plane.

Table 1 displays the time t'_B and position of maximum surface elevation (x'_B, z'_B) at the breaking point at $y'=0$ for the five values of k. The breaking point corresponds to the instant when the front face of the wave reaches a vertical tangent before the wave crest overturns. We observe that t'_B, x'_B and z'_B increase with k (as suggested in figure 5), and these differences in time evolution and wave shape are attributable to wave refraction and focusing over the ridge, as discussed below.

Figure 8 shows a comparison of breaker shapes computed at $y'=0$ with the three-dimensional model and the two-dimensional fully nonlinear potential flow model of Grilli & Subramanya (1996) and Grilli *et al.* (1997). The latter model, which has been extensively tested and validated against both theoretical and experimental results, is run for a bottom slope $s=1{:}15$, corresponding to the geometry of the cross-section $y'=0$ in the three-dimensional NWT. The same incident wave, i.e. a 'Tanaka' solitary wave of height $H'_0=0.6$ and speed $c'_0=1.25$, is specified in both models. Note, a finer resolution is used in the x-direction in the two-dimensional model ($\Delta x'_0=0.1$). The comparison is shown for the five values of k, at slightly different times, for which the two- and three-dimensional waves have similar free-surface profiles near the breaker

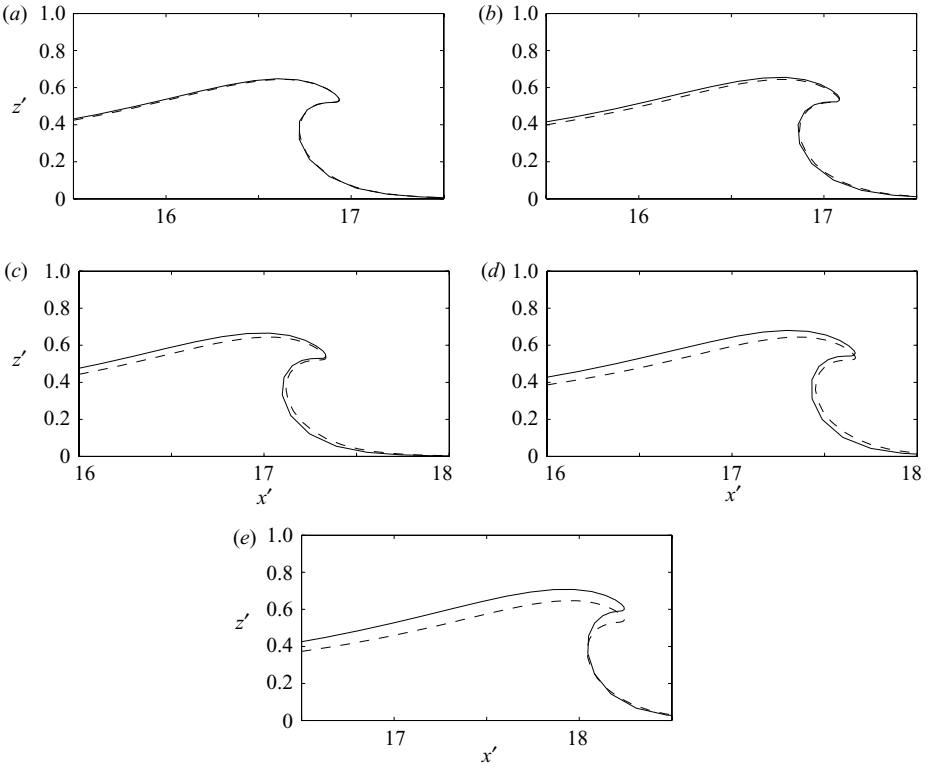

FIGURE 8. Comparison of two-dimensional (dashed line) and three-dimensional (solid line) results at similar stages of wave overturning: (*a*) $t' = 8.248, 8.299$ ($k = 0.1$), (*b*) $t' = 8.248, 8.397$ ($k = 0.17$), (*c*) $t' = 8.248, 8.563$ ($k = 0.25$), (*d*) $t' = 8.248, 8.796$ ($k = 0.34$), (*e*) $t' = 8.218, 9.243$ ($k = 0.5$), for the two- and three-dimensional waves, respectively. For the three-dimensional results, only the vertical cross-section at $y' = 0$ is represented. The two-dimensional wave profile is shifted forward by $\delta x' = 0.086$ in (*a*), 0.233 in (*b*), 0.484 in (*c*), 0.816 in (*d*) and 1.443 in (*e*) along the x-axis.

jets. Furthermore, to allow for a direct comparison of breaker jet geometry, the two-dimensional profiles are shifted forward by $\delta x'$ ($\delta x' = 0.086$, 0.233, 0.484, 0.816, 1.443 for $k = 0.1$, 0.17, 0.25, 0.34, 0.5, respectively), to make them approximately coincide with the three-dimensional profiles. For $k = 0.1$, figure 8(*a*) shows that the two- and three-dimensional wave profiles are quite close to each other. As k increases, however, the three-dimensional wave profiles exhibit a higher back slope and a more arched front face than the two-dimensional profiles. Similar observations were made by Xue *et al.* (2001) for periodic deep-water breakers, when considering domains of large width.

Values of $\delta x'$ given above clearly indicate that wave breaking takes longer to develop in three dimensions than in two dimensions, for the specified maximum bottom slope. Also, the more three-dimensional the bottom topography (i.e. the larger k), the longer it takes for breaking to develop. The differences in spatial and temporal evolutions of the two- and three-dimensional waves are also illustrated by the values of x'_B (and t'_B) given in table 1 for $s = 1{:}15 \simeq 0.067$. Two-dimensional results for $s = 0.028$ and 0.052, corresponding to the bottom slopes at $y' = \pm 4$ and ± 2 in the three-dimensional case with $k = 0.25$, are also given in table 1. In these two-dimensional cases with smaller slopes, wave breaking occurs later than in three-dimensions (the difference in x'_B

is $\delta x'_B = 0.792$ for $s = 0.052$, and it is $\delta x'_B = 4.364$ for $s = 0.028$). These significant differences for wave shoaling and breaking over different slopes explain why, in three dimensions, (*i*) wave breaking is delayed as k increases, and (*ii*) the middle portion of the wave takes longer to break than in a purely two-dimensional configuration.

Values of z'_B in table 1 also show that, the larger the value of k, the stronger the wave focusing towards the centre owing to the transverse depth variations. This is supported by figure 8, which clearly shows the increased elevations of three-dimensional waves relative to the two-dimensional solution at $y' = 0$. At the same time, since wave breaking takes longer to develop and occurs for smaller depth, as k increases, this results in larger values of the breaker height ratio z'_B/h'_B. The values of z'_B/h'_B that we obtained (for three-dimensional waves) are in the range of typical values for plunging breakers (according to e.g. Grilli *et al.* 1997), and this is clearly seen in figure 6. Note, however, that we were unable to compute the solution until an advanced stage of wave overturning for $k = 0.5$, which gives the largest ratio z'_B/h'_B in table 1.

The low global errors found for these computations (figure 7) give little indication as to how well the more important highly energetic parts of the flow such as the plunging jets are modelled. In particular, the calculation of particle accelerations is very sensitive to local variations of the boundary geometry and, therefore, inaccuracies can be observed in the overturning region. We have experienced such errors in our computations even though global errors are quite small. We believe, however, these errors have little impact on the overall solution, since our results show remarkable similarities when comparing two- and three-dimensional wave breaking. Moreover, we have obtained satisfactory results for velocity and accelerations fields in smooth areas of the free surface (see figures 12*b* and 13*b*).

4.2. *Solitary wave breaking over a sloping ridge: configuration* $k = 0.25$

We now focus our attention on the case $k = 0.25$ and conduct a more detailed study of three-dimensional wave overturning. This case is of particular interest because, as shown in figure 6(*c*), the solution exhibits a well-developed localized plunging jet and the computation can be run over a sufficiently long time before breaking down. As the overturning process propagates laterally to the sidewalls ($y' = \pm 4$), the projected water forms a tongue-shaped jet, which is clearly a three-dimensional effect. The transverse variation of the jet is smooth, as is that of the bottom topography.

Computations break down a few time steps after $t' = 9.142$ owing to node convergence in the plunging jet and because elements in this region become too distorted; results, however, remain accurate until that stage (figure 7). We point out that the numerical instabilities due to node convergence (i.e. situations of quasi-singular integrals in the BIEs; see e.g. Grilli & Subramanya 1994) are somewhat different from the so-called sawtooth instabilities. These have been commonly observed in numerical simulations of water waves and are removed by means of smoothing techniques (e.g. Longuet-Higgins & Cokelet 1976; Xue *et al.* 2001). Such sawtooth instabilities have never been observed in all cases studied here. Incidentally, the present calculations span several hundred time steps and the CPU time is $O(10)$ min per time step for $N_\Gamma = 6022$, on a single processor of a Compaq Alpha GS160 computer.

Figure 9 shows the vertical cross-sections of the free surface in the middle ($y' = 0$) and at the sidewall ($y' = \pm 4$) locations in the tank, for times $t' = 7.890$, 8.244, 8.498, 8.827, 9.142. Because of the large differences in depth variations and resultant wave focusing, the wave profile at $y' = 0$ has developed well into overturning, with a prominent plunging jet, while the profile at $y' = \pm 4$ remains single-valued. Figure 9(*a*)

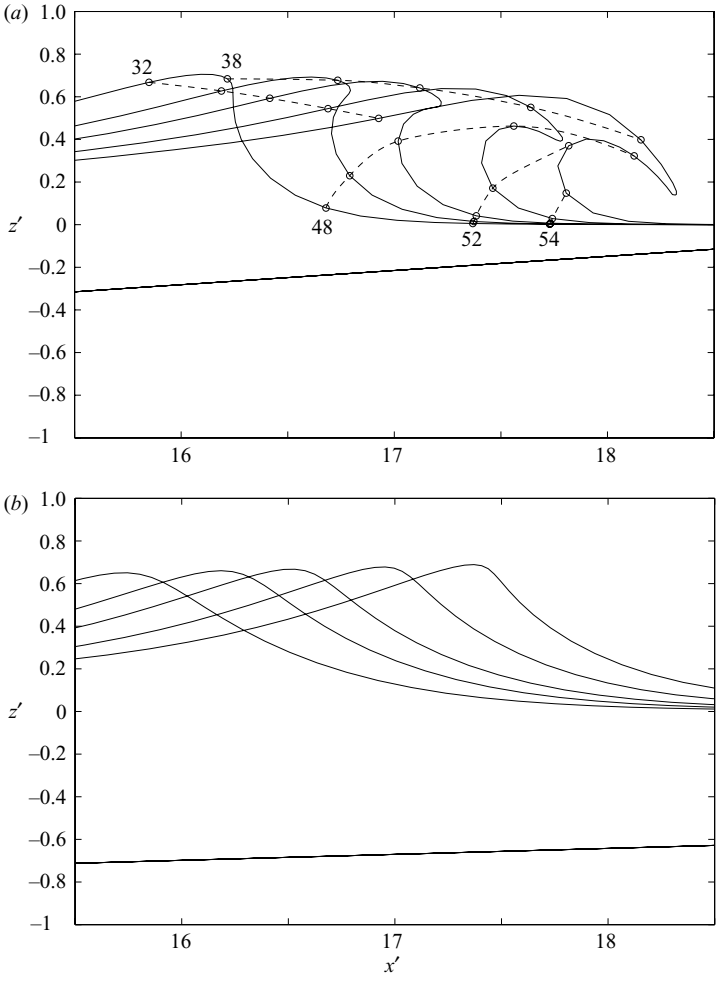

FIGURE 9. $k = 0.25$. Vertical cross-sections along the x-axis, in the middle (a) $y' = 0$ and at the sidewalls (b) $y' = \pm 4$: wave profiles at $t' = 7.890, 8.244, 8.498, 8.827, 9.142$ (left to right, solid line); particle paths (dashed line). The straight line represents the bottom profile. The resolution in the x-direction is 61 particles and particle numbers are indicated at the beginning of each path.

shows that the wave reaches its maximum height $H' \simeq 0.71$ near the breaking point ($t' = 7.890$) with the crest located at $x' = 16.2$. The surface elevation then decreases gradually as the jet of water is projected forward. More precisely, as indicated in table 3, the wave height still increases slightly beyond the breaking point to reach a maximum around $t' = 8.827$. We point out that the problem of solitary wave focusing, e.g. over a ridge as presented here, can be analysed in the framework of ray theory. Miles (1977) and Pedersen (1994) applied such a theory to solitary waves, and examined the transverse propagation of disturbances on solitary waves. It would be of interest, in the future, to compare the present results with these theories.

The sequence of wave profiles in figure 9(a) is in good qualitative agreement with existing results of two-dimensional numerical simulations of overturning waves (e.g. on finite depth by New *et al.* 1985; in deep water by Dommermuth *et al.* 1988; over slopes by Grilli *et al.* 1997). This supports the standard view that the general features

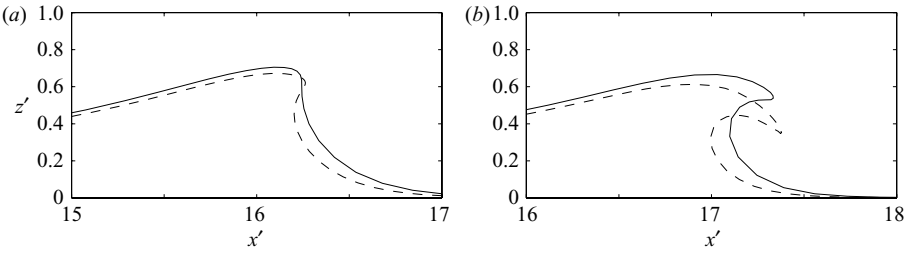

FIGURE 10. $k = 0.25$. Comparison of two-dimensional (dashed line) and three-dimensional (solid line) results at (*a*) $t' = 7.890$ and (*b*) $t' = 8.560$. For the three-dimensional results, only the vertical cross-section at $y' = 0$ is represented.

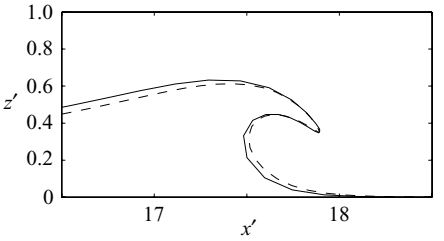

FIGURE 11. $k = 0.25$. Comparison of two-dimensional (dashed line) and three-dimensional (solid line) results at similar stages of wave overturning: $t' = 8.560, 8.889$ for the two-, three-dimensional wave, respectively. The two-dimensional wave profile is shifted forward by $\delta x' = 0.514$ along the x-axis.

of wave overturning do not vary much with the physical situation that has caused it. A more detailed comparison of wave-breaking profiles obtained using the two- and three-dimensional numerical models for $k = 0.25$ is shown in figures 10 and 11. At a given time, the crests of both two- and three-dimensional waves are roughly located at the same x-location. As expected from the discussions in § 4.1, however, in figure 10, breaking occurs earlier in two dimensions owing to differences in wave evolution between the middle and the sides of the tank in the three-dimensional case. Figure 11 shows the same comparison, but for similar late stages of wave overturning, occurring at different times in the two models (the two-dimensional wave profile is shifted by $\delta x' = 0.514$ to allow for a better comparison). Surprisingly, at this stage, the breaker jets of the two- and three-dimensional waves match almost perfectly. Finally, we also found that we can fit ellipses to the interior of the two- and three-dimensional jets (i.e. 'the pipe') in figure 11 which, as in the local analytical solution of New (1983), come out approximately with a $\sqrt{3}$ aspect ratio and are inclined at about 30°.

4.3. *Kinematics of three-dimensional overturning waves: configuration* $k = 0.25$

We analyse the effects of three-dimensional breaking on wave kinematics for $k = 0.25$. We anticipate that the bottom topography is an important factor governing the internal dynamics. As shown above, the solitary wave starts overturning in the middle of the domain where the bottom slope is the steepest and so we should expect significant variations of the wave kinematics in this part of the domain. In our computations, the particle velocity $\boldsymbol{u} = \nabla\phi = (u_x, u_y, u_z)$ and acceleration $\boldsymbol{a} = \mathrm{D}\boldsymbol{u}/\mathrm{D}t = (a_x, a_y, a_z)$ on the free surface are expressed using polynomial interpolation in a local curvilinear coordinate system defined at each node (see Grilli *et al.* 2001; Fochesato *et al.* 2005). For interior points, we use the integral formulae (2.7) and (2.9). Because of this

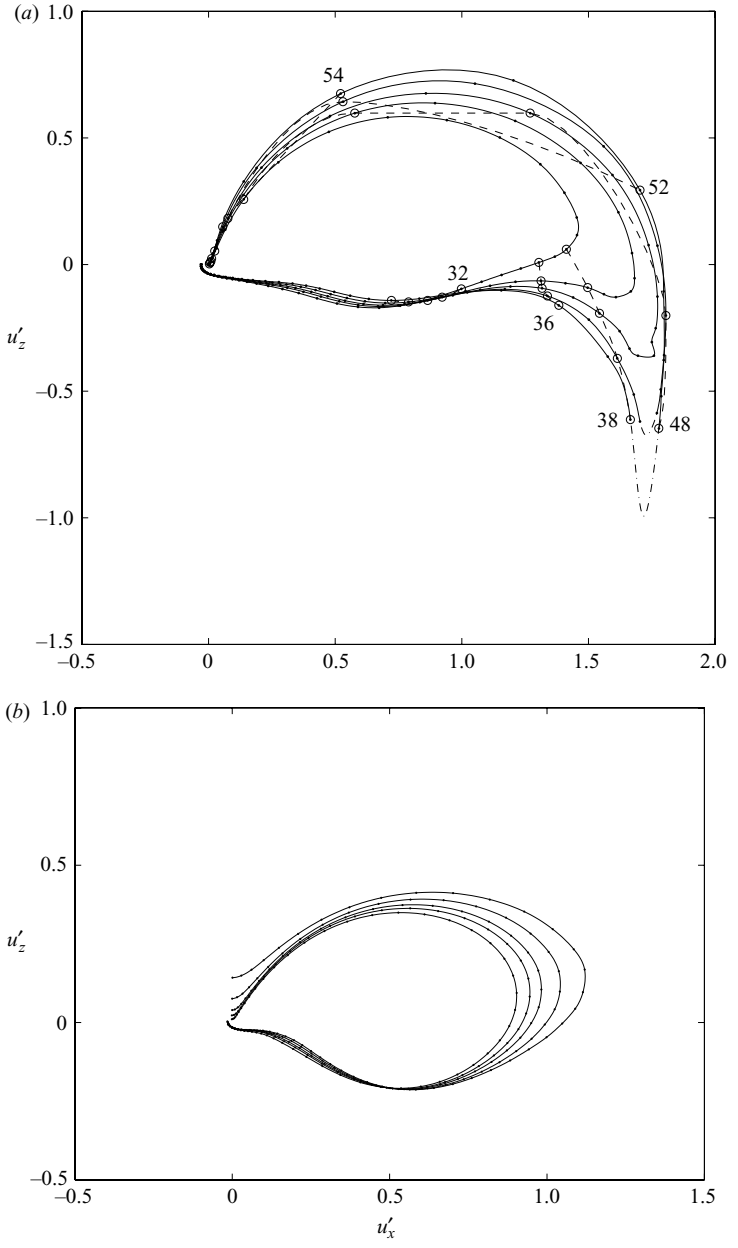

FIGURE 12. $k = 0.25$. Surface velocity portraits in the (u_x, u_z)-plane for (*a*) $y' = 0$ and (*b*) $y' = \pm 4$ at $t' = 7.890, 8.244, 8.498, 8.827, 9.142$: velocity curves (solid line); regions of significant numerical error (dashed-dotted line); particle trajectories (dashed line). The innermost/outermost curve corresponds to the earliest/latest time. Particle numbers are indicated at the end of each trajectory.

integral formulation, the calculation of field variables is expected to be more accurate within the domain than on its boundary, where differentiation is used.

Following New *et al.* (1985), we found it useful to represent wave kinematics on the free surface using velocity and acceleration plane portraits. Figure 12 shows the

t'	$\lvert\boldsymbol{u}'\rvert_{max}$	$(u'_{max})_x$	$(u'_{max})_y$	$(u'_{max})_z$	$\lvert\boldsymbol{a}'\rvert_{max}$	$(a'_{max})_x$	$(a'_{max})_y$	$(a'_{max})_z$
7.890	1.466	1.454	0.000	0.186	2.503	0.818	0.000	−2.365
8.244	1.683	1.682	0.000	−0.054	2.745	2.608	0.000	−0.858
8.498	1.784	1.766	0.000	−0.251	5.235	3.337	±2.021	−3.491
8.827	1.860	1.771	0.000	−0.569	5.311	3.063	±3.606	−2.413
9.142	1.950	1.720	0.000	−0.919	5.769	5.635	±0.476	−1.144

TABLE 2. $k = 0.25$. Maximum values of the surface velocity/acceleration magnitudes and corresponding components at $t' = 7.890, 8.244, 8.498, 8.827, 9.142$. Note that, owing to the symmetry about $y' = 0$, there are two values of same magnitude and opposite signs for $(a'_{max})_y$ (and $y'_{a_{max}}$ in table 3).

t'	z'_{max}	$x'_{z_{max}}$	$(z'/h')_{max}$	$x'_{u_{max}}$	$y'_{u_{max}}$	$z'_{u_{max}}$	$x'_{a_{max}}$	$y'_{a_{max}}$	$z'_{a_{max}}$
7.890	0.7062	16.094	2.564	16.242	0.000	0.637	16.242	0.000	0.637
8.244	0.7088	16.486	2.843	16.787	0.000	0.614	16.705	0.000	0.427
8.498	0.7099	16.802	3.111	17.176	0.000	0.548	17.074	±0.934	0.600
8.827	0.7107	17.175	3.495	17.694	0.000	0.425	17.380	±1.713	0.641
9.142	0.7101	17.556	3.991	18.307	0.000	0.195	18.066	±1.354	0.446

TABLE 3. $k = 0.25$. Position (x, z) and height to depth ratio for the maximum surface elevation, and position (x, y, z) of maximum velocity/acceleration magnitudes on the free surface at $t' = 7.890, 8.244, 8.498, 8.827, 9.142$.

time evolution of particle velocities in the (u_x, u_z)-plane for $y' = 0$ and $y' = \pm 4$. For comparison, the linear phase speed in shallow water $c = \sqrt{gh_0}$ denotes the unit speed in our non-dimensionalization. Because of the moderate resolution in our computations and for graphical clarity purpose, we used cubic spline interpolation to estimate the velocity values between nodes. This is consistent with the order of approximation specified in our BEM method for space discretization. A single curve represents particle velocities on the free surface at a given time. The innermost/outermost curve corresponds to the earliest/latest time. Regions of larger numerical errors around the tip of the jet are represented by a dashed-dotted line.

We note that the velocity profiles for $y' = 0$ look very similar to those obtained by New *et al.* (1985) for two-dimensional periodic breakers on constant depth. In particular, the most prominent feature of the diagram is the development of a jet in the bottom right-hand corner. The corresponding particles are approaching free fall and have the largest velocities with an almost-constant horizontal component. The accumulation of particles near the origin indicates the absence of motion as we move away from the crest of the overturning solitary wave. The maximum velocity occurs near the tip of the plunging jet and is almost $2c$ at $t' = 9.142$ (table 2). This is roughly 1.5 times c_0 the initial speed of the solitary wave. Velocities at $y' = \pm 4$ do not exceed c much (figure 12*b*). The corresponding diagram is close to that of a steadily progressing solitary wave.

Similarly, figure 13 plots the time evolution of particle accelerations in the (a_x, a_z)-plane for $y' = 0$ and $y' = \pm 4$. Significant numerical errors are observed for particles located inside the breaking loop and around the tip of the jet. Such errors were discussed in § 4.1 and can be reduced by increasing the grid resolution. It can be seen in

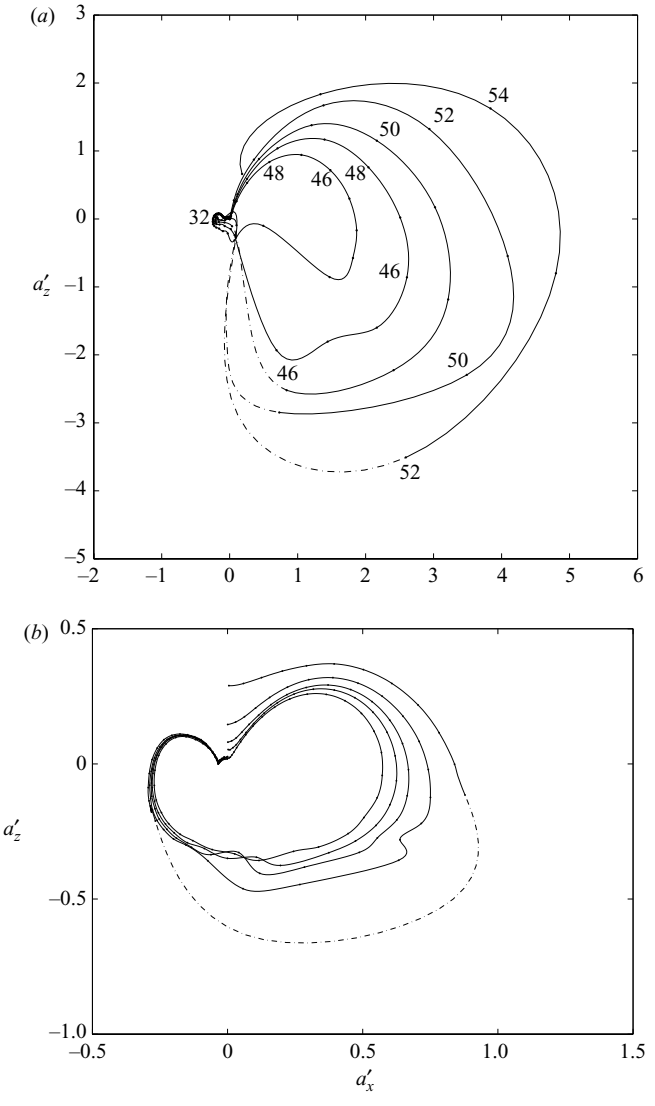

FIGURE 13. $k = 0.25$. Surface acceleration portraits in the (a_x, a_z)-plane for (*a*) $y' = 0$ and (*b*) $y' = \pm 4$ at $t' = 7.890, 8.244, 8.498, 8.827, 9.142$: acceleration curves (solid line); regions of significant numerical error (dashed-dotted line). Particles are also marked.

figure 13(*a*) that two-dimensional magnitudes (i.e. in the vertical plane) as high as almost $5g$ occur at $t' = 9.142$ on the front face where the curvature is large. At the sidewalls, the non-overturning free surface exhibits accelerations typically less than g (figure 13*b*). Larger numerical inaccuracies occur for the last recorded time, owing to distortions of elements on the sidewalls as the wave becomes steeper at the sides. As pointed out in Peregrine, Cokelet & McIver (1980), at any point on the free surface, the particle acceleration is given by the equation of motion

$$\frac{\mathrm{D}\boldsymbol{u}}{\mathrm{D}t} = -\frac{1}{\rho}\nabla p + \boldsymbol{g}. \tag{4.1}$$

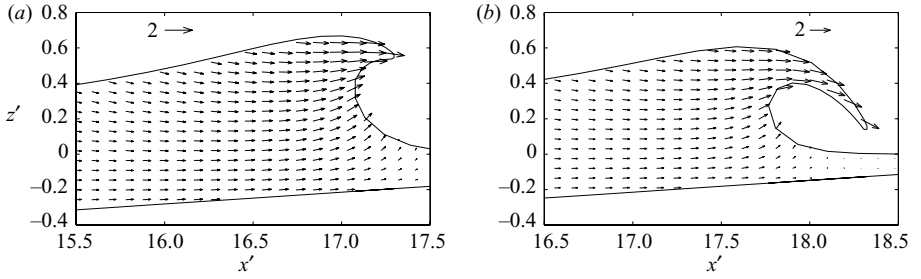

FIGURE 14. $k = 0.25$. Internal velocity components (u_x, u_z) at (a) $t' = 8.542$ and (b) $t' = 9.142$. In the (x, z)-plane, the maximum velocity magnitude is $|\boldsymbol{u}'|_{max} = 1.756$ at $t' = 8.542$ and $|\boldsymbol{u}'|_{max} = 1.974$ at $t' = 9.142$.

Since the pressure gradient is normal to the surface and $\boldsymbol{g}$ is downwards, the general direction (e.g. off- or on-shore) of $\mathrm{D}\boldsymbol{u}/\mathrm{D}t$ is determined by the slope of the surface. This property is reproduced well here and generalizes to the acceleration field within the flow (see below).

We also note that, while the maximum velocity on the surface occurs in the cross-section $y' = 0$ (with zero y-component as in the two-dimensional case), the maximum acceleration exhibits a significant transverse component a_y, which can be of the same order of magnitude as a_x or a_z (see Tables 2 and 3). Total accelerations (i.e. three-dimensional) as high as almost $6g$ are thus observed at $t' = 9.142$. We point out that two maxima are observed for the acceleration field, which are located symmetrically about $y' = 0$ and with components a_y of opposite signs. These are directed towards the sides, i.e. $a_y > 0$ (respectively $a_y < 0$) for $y > 0$ (respectively $y < 0$). It seems that these two maxima occur on the front face of the wave, near the portion of the wave crest which has just started overturning at the sides. The transverse acceleration, being moderately large and directed to the sides, may be related to the fact that, since the wave gains height more rapidly at the centre, there is extra pressure (hydrostatic to the first approximation) which accelerates water away from the centreline in the main body of the wave. In the lower portions at the front of the wave, this may not be so, since the low front of the wave can travel faster in the deeper water at the sides of the tank, so that transverse acceleration there will be towards the lower front of the wave at the centre. Indeed, as discussed below, figures 16–18 show that water has been accelerated towards the centre.

Figure 14 displays the internal velocity components (u_x, u_z) in the middle $(y' = 0)$ at $t' = 8.542$ and $t' = 9.142$ after the breaking point. The interior points are chosen equally spaced by $\Delta x_i' = 0.10$ and $\Delta z_i' = 0.05$ along the x- and z-axes, respectively. Outside the overturning region, the quasi-uniformity of the velocity distribution along the depth is clearly shown. This is expected for a very long wave such as a solitary wave. There is also an overall uniformity in direction parallel to that of wave propagation. Velocities increase and exhibit more variations in the vertical direction as we enter the breaker jet, as a result of flow focusing towards the jet in the vertical plane.

By contrast, the corresponding acceleration components (a_x, a_z) have appreciable values only in the region adjacent to the wavefront face (figure 15). The existence of such a region is necessary to accelerate the water near the surface, which is projected forward in a jet. In particular, large variations in acceleration are observed for particles in the close neighbourhood of the surface and within 'the pipe' where the curvature

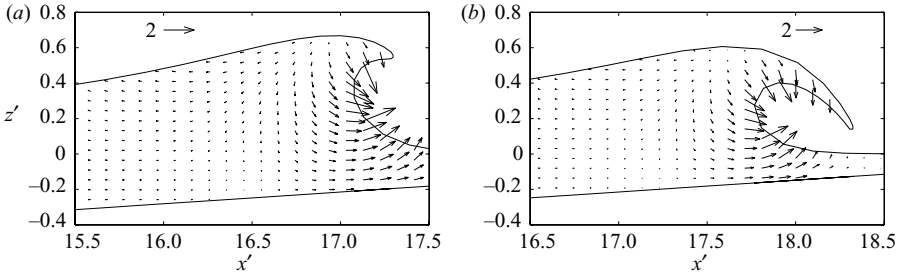

FIGURE 15. $k=0.25$. Internal acceleration components (a_x, a_z) at (*a*) $t'=8.542$ and (*b*) $t'=9.142$. In the (x, z)-plane, the maximum acceleration magnitude is $|\boldsymbol{a}'|_{max}=2.281$ at $t'=8.542$ and $|\boldsymbol{a}'|_{max}=2.204$ at $t'=9.142$.

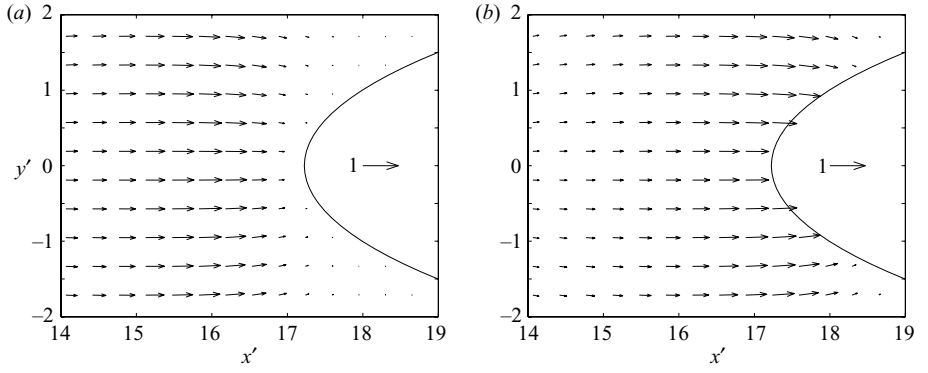

FIGURE 16. $k=0.25$. Internal velocity components (u_x, u_y) at depth $z'=-0.2$ at (*a*) $t'=7.973$ and (*b*) $t'=9.142$. In the (x, y)-plane, the maximum velocity magnitude is $|\boldsymbol{u}'|_{max}=0.651$ at $t'=7.973$ and $|\boldsymbol{u}'|_{max}=0.694$ at $t'=9.142$. The ratio of maximum $|u_y|$ to maximum $|u_x|$ is $|u_y|_{max}/|u_x|_{max}=0.085$ at $t'=7.973$ and $|u_y|_{max}/|u_x|_{max}=0.112$ at $t'=9.142$. The curve at the $+x$ extremity represents the cross-section of the sloping ridge.

is the largest (compare surface values in figure 13*a* to internal values in figure 15*b*). Further examination reveals that a transition zone takes place beneath the back slope of the wave, more precisely here at $x' \simeq 16.7$ ($t'=8.542$) and $x' \simeq 17.5$ ($t'=9.142$), between low backward accelerations and high forward accelerations. The location of this transition zone coincides with the location of the wave crest at $y'=\pm 4$, which has not yet overturned. Our numerical results are in good qualitative agreement with those obtained by Peregrine *et al.* (1980), who gave a detailed discussion of accelerations in two-dimensional breakers. These authors also identified the region of high accelerations as the steep front portion of the wave just below the crest, and the region of low accelerations at the wave crest and its back.

Transverse variations of the wave kinematics are shown in figures 16 and 17 where we plot the internal velocity and acceleration components (u_x, u_y) and (a_x, a_y), respectively, in a horizontal cross-section at depth $z'=-0.2$ ($\Delta x_i'=0.35$ and $\Delta y_i'=0.38$). The solutions at $t'=7.973$ (near the breaking point) and $t'=9.142$ (latest computed stage) are considered. As indicated in figure 16, the propagation of the solitary wave is associated with a forward displacement of water beneath the surface. The wave-induced velocity field is appreciable only in the vicinity of the wave crest position. Velocities rapidly decay as we tend to both x extremities of the tank. A remarkable feature is that the fluid motion remains primarily longitudinal, but

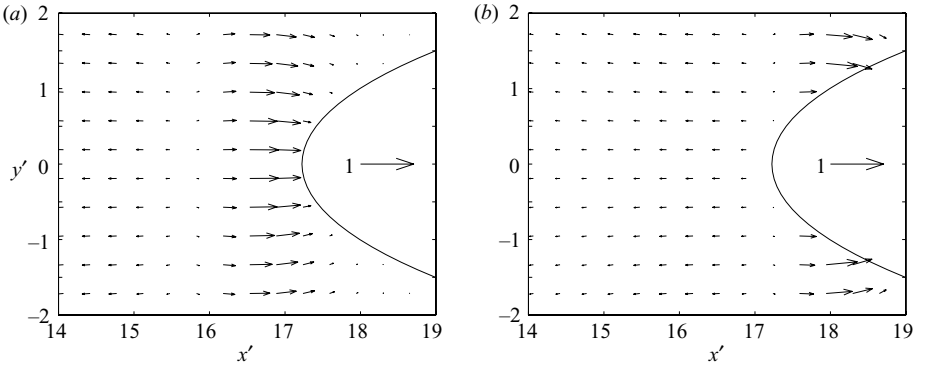

FIGURE 17. $k = 0.25$. Internal acceleration components (a_x, a_y) at depth $z' = -0.2$ at (a) $t' = 7.973$ and (b) $t' = 9.142$. In the (x, y)-plane, the maximum acceleration magnitude is $|\boldsymbol{a}'|_{max} = 0.542$ at $t' = 7.973$ and $|\boldsymbol{a}'|_{max} = 0.589$ at $t' = 9.142$. The ratio of maximum $|a_y|$ to maximum $|a_x|$ is $|a_y|_{max}/|a_x|_{max} = 0.096$ at $t' = 7.973$ and $|a_y|_{max}/|a_x|_{max} = 0.178$ at $t' = 9.142$. The curve at the $+x$ extremity represents the cross-section of the sloping ridge.

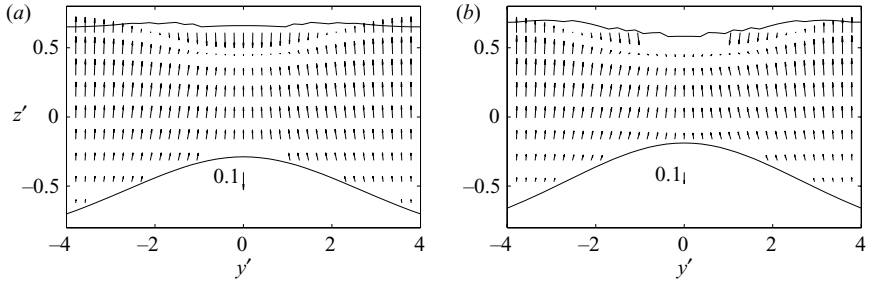

FIGURE 18. $k = 0.25$. Internal velocity components (u_y, u_z) at (a) $t' = 7.973$ $(x' = 15.9)$ and (b) $t' = 9.142$ $(x' = 17.4)$. In the (y, z)-plane, the maximum velocity magnitude is $|\boldsymbol{u}'|_{max} = 0.100$ at $t' = 7.973$ and $|\boldsymbol{u}'|_{max} = 0.160$ at $t' = 9.142$. The ratio of maximum $|u_y|$ to maximum $|u_z|$ is $|u_y|_{max}/|u_z|_{max} = 0.301$ at $t' = 7.973$ and $|u_y|_{max}/|u_z|_{max} = 0.357$ at $t' = 9.142$. The upper and lower curves represent the transverse profiles of the free surface and sloping ridge, respectively. The vertical scale is exaggerated.

small transverse variations due to focusing of the flow by the ridge can be seen in figure 16(b). While remaining relatively small, these transverse variations increase with time. The ratio of maximum $|u_y|$ to maximum $|u_x|$ increases from $|u_y|_{max}/|u_x|_{max} = 0.085$ to 0.112 between $t' = 7.973$ and $t' = 9.142$.

We also observe that no significant change in the maximum of u_x occurs during the wave evolution. This suggests that the mean wave speed is almost constant and the wave does not slow down as it travels up the sloping ridge. This result is not really unexpected since the incident solitary wave is very energetic owing to its large amplitude. In addition, the wave dynamics are strongly disturbed by the bottom topography only in the middle of the tank where the slope is the steepest. The same remarks can be made when examining the acceleration field. The transition zone, as mentioned earlier, between small negative accelerations and large positive accelerations is clearly indicated by a transverse dotted line in figure 17. Similar results were obtained for horizontal cross-sections at greater depths.

Three-dimensional effects are especially conspicuous in figures 18 and 19 which show the internal velocity components (u_y, u_z) and the corresponding acceleration

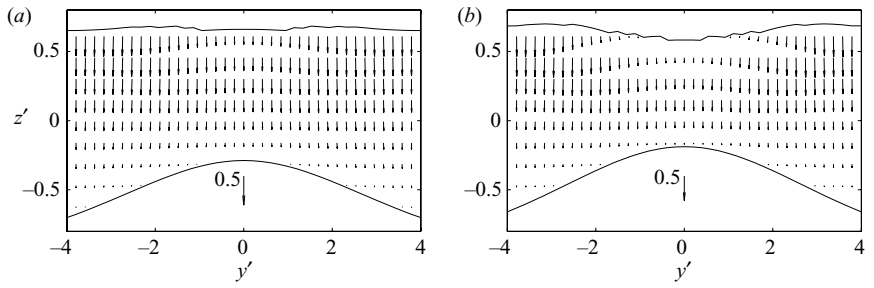

FIGURE 19. $k=0.25$. Internal acceleration components (a_y, a_z) at (a) $t'=7.973$ $(x'=15.9)$ and (b) $t'=9.142$ $(x'=17.4)$. In the (y,z)-plane, the maximum acceleration magnitude is $|\boldsymbol{a}'|_{max}=0.343$ at $t'=7.973$ and $|\boldsymbol{a}'|_{max}=0.420$ at $t'=9.142$. The ratio of maximum $|a_y|$ to maximum $|a_z|$ is $|a_y|_{max}/|a_z|_{max}=0.078$ at $t'=7.973$ and $|a_y|_{max}/|a_z|_{max}=0.127$ at $t'=9.142$. The upper and lower curves represent the transverse profiles of the free surface and sloping ridge respectively. The vertical scale is exaggerated.

components (a_y, a_z), respectively. Vertical cross-sections at $x'=15.9$ for $t'=7.973$ and at $x'=17.4$ for $t'=9.142$ are presented ($\Delta y_i'=0.21$ and $\Delta z_i'=0.15$). These locations, which correspond roughly to the location of the wave crest at the sidewalls ($y'=\pm 4$), are chosen to ensure a single-valued profile of the free surface along the transverse axis. It can be seen that both velocities and accelerations exhibit quite small y- and z-components, particularly at the early stage of breaking $t'=7.973$. Components u_z and a_z also decrease rapidly with z, attaining negligible values near the bottom and sidewalls where the depth is the greatest. This is a typical effect in shallow water, which results from the flattening of the orbital motion of fluid particles near the bottom.

As depicted in figure 18, the velocity field is mainly directed upward with a dominant vertical component. Nevertheless, the maximum values of $|u_y|$ and $|u_z|$ are found to differ only by a moderate factor ($|u_z|_{max}/|u_y|_{max}=2.803$ at $t'=9.142$). The development of wave breaking is indicated by the flow convergence above the top of the ridge, and by the decay of velocities just beneath the surface as we tend laterally to $y'=0$. In the middle of the tank, a localized zone of negative u_z can be identified near the surface. Large negative values of u_z are observed in this zone for $t'=7.973$ because the vertical cross-section at $x'=15.9$ is located well behind the wave crest (figure 18*a*). For $t'=9.142$, the vertical cross-section is chosen at $x'=17.4$, which is close to the position of maximum surface elevation. Therefore, small negative values of u_z are obtained since the flow is almost horizontal near the surface at this position (figure 18*b*).

Note that the wave crest develops a lower part around $y'=0$ as the jet of water is projected forward and plunges down. Figure 19 shows that the acceleration field is also predominantly vertical, but directed downward owing to the influence of gravity. Accelerations decrease so rapidly with z that scattering by the ridge is not really observed. As wave breaking develops, the variations of a_y become more significant with respect to a_z.

Overall, our calculations of surface and internal kinematics of overturning waves are consistent in magnitude and direction with the PIV laboratory measurements of Perlin, He & Bernal (1996), Skyner (1996) and Chang & Liu (1998), for two-dimensional deep-water breaking waves, as well as with the Navier–Stokes (NS) simulations of breaking waves by Chen *et al.* (1999), Lachaume *et al.* (2003) and Biausser *et al.* (2004).

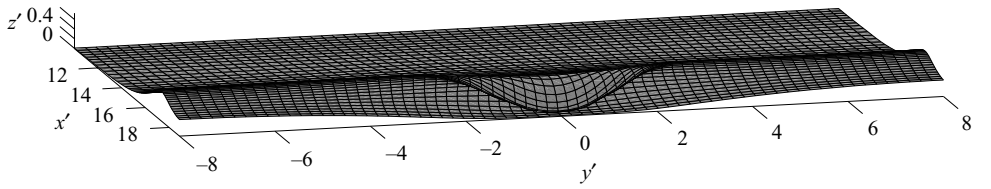

FIGURE 20. $k = 0.25$. Wave profile at $t' = 9.268$ in a domain of length $19h_0$ and width $16h_0$. The initial solitary wave is of height $H_0' = 0.6$.

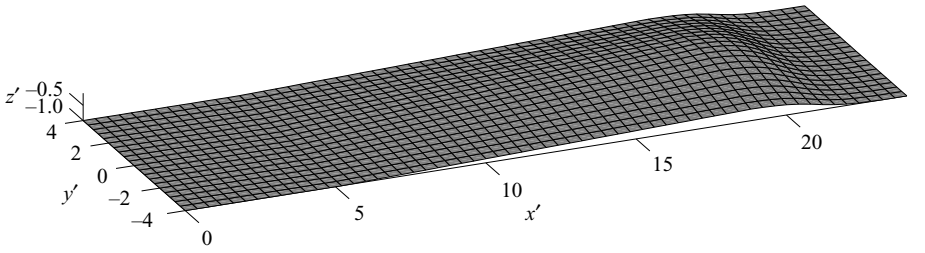

FIGURE 21. Bottom topography specified as a 1:15 sloping ridge with $k = 0.25$ for $5.225 < x' < 19$ and then a decaying tanh-like profile for $19 \leqslant x' \leqslant 24$.

4.4. *Sensitivity to domain size and configurations with varying incident wave heights*

We examine briefly the sensitivity of computations to domain size, and present some results for varying incident wave heights. Recall that no-flow Neumann boundary conditions are specified at both the sides and extremities of the NWT, and so the question arises as to whether the similarities between two- and three-dimensional overturning waves persist when varying the size of the domain. It is also of interest to examine the differences in wave breaking for varying incident wave heights since, according to two-dimensional studies, this is an important factor controlling breaking characteristics.

For a domain of the same length $19h_0$ as previously, but of double the width ($-8 \leqslant y' \leqslant 8$), wave overturning computed for $-2 \leqslant y' \leqslant 2$ appears very similar to that in the case with a smaller domain width $8h_0$ (compare figure 20 to figure 6*c*). Vertical cross-sections through breaker jets at $y' = 0$ (not shown here) are in close agreement. Wave behaviour at the edges in figure 20 comes within 1% of the corresponding two-dimensional solution. We have also run simulations for even longer domains (e.g. of length $24h_0$) and results (not shown here) reveal quite similar features.

So far, all of our simulations have been conducted for solitary waves of initial height $H_0' = 0.6$. Figures 22 and 23 show wave profiles in the latest stages of overturning for $H_0' = 0.3$ and $H_0' = 0.7$, respectively. In both cases, the domain has the following characteristics: width $8h_0$, bottom topography with a 1:15 sloping ridge ($k = 0.25$). Note, however, that a longer domain is specified for $H_0' = 0.3$ ($0 \leqslant x' \leqslant 24$), with bottom topography as depicted in figure 21, because of the longer evolution towards breaking in this case. For $H_0' = 0.3$, the wave crest is initially located at $x_0' = 6.400$ and the breaking point occurs at $t_B' = 10.881$ for $y' = 0$, with maximum surface elevation at $(x_B', z_B', z_B'/h_B') = (18.691, 0.412, 4.029)$. For $H_0' = 0.7$, we have $x_0' = 5.325$, $t_B' = 7.250$ and $(x_B', z_B', z_B'/h_B') = (15.164, 0.782, 2.318)$. We can therefore obtain the distance of propagation up to the breaking point for $H_0' = 0.3, 0.6, 0.7$ ($k = 0.25$) as $d_B' = x_B' - x_0' = 12.291, 10.360, 9.839$, respectively. As expected, the smaller the

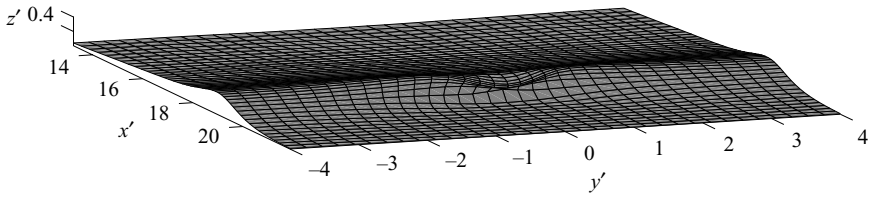

FIGURE 22. $k = 0.25$. Wave profile at $t' = 11.523$ for a 'Tanaka' solitary wave of initial height $H_0' = 0.3$. The domain is of length $24h_0$ and width $8h_0$.

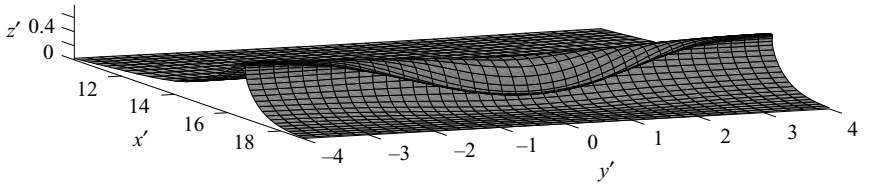

FIGURE 23. $k = 0.25$. Wave profile at $t' = 8.477$ for a 'Tanaka' solitary wave of initial height $H_0' = 0.7$. The domain is of length $19h_0$ and width $8h_0$.

initial wave amplitude, the longer it takes for breaking to develop. For $H_0' = 0.7$, wave breaking characteristics are similar to those for $H_0' = 0.6$ with $k = 0.17$. Small-amplitude waves evolve more slowly towards breaking than large-amplitude waves, but their shape seems to be more affected by the bottom topography. Indeed, the breaker height ratio for $H_0' = 0.3$ is almost twice as large as that for $H_0' = 0.7$. This may be related to the fact that, since breaking of small waves occurs further up the beach, there is more time for refraction and focusing of wave energy towards the centre.

In figure 24, we show the transverse variation of the ridge geometry and that of the wave crest at the breaking point $x' = x_B'$, for $H_0' = 0.3$, 0.6 and 0.7. These variations are correlated to some extent. In particular, for $H_0' = 0.3$, there is a relatively strong focusing of the wave at the breaking point, which occurs in the shallowest water, near the maximum elevation of the ridge in figure 24(*a*). By contrast, for $H_0' = 0.7$, the breaking point occurs in deeper water and wave focusing is so weak that it is hardly noticeable in figure 24 (*c*). Specifically, for $H_0' = 0.3$, the relative difference in surface elevation between $y' = 0$ and $y' = \pm 4$ is 32%, while it is only 4% for $H_0' = 0.7$.

5. Conclusions

The three-dimensional NWT of Grilli *et al.* (2001), based on an accurate BEM and an efficient time-stepping scheme, has been used to investigate physical aspects of the shoaling and overturning of solitary waves over a sloping ridge with a lateral modulation.

The three-dimensional aspects of the problem have been examined by varying the transverse geometry of the bottom, the domain size and incident wave height. A detailed analysis of the dynamics and kinematics (both on the free surface and within the flow) of plunging breakers has been performed. We have observed three-dimensional effects on wave profiles and surface kinematics similar to those observed by Xue *et al.* (2001) for periodic overturning waves in deep water. The transverse variation of the bottom turns out to be an important factor controlling the geometry and type of breaking.

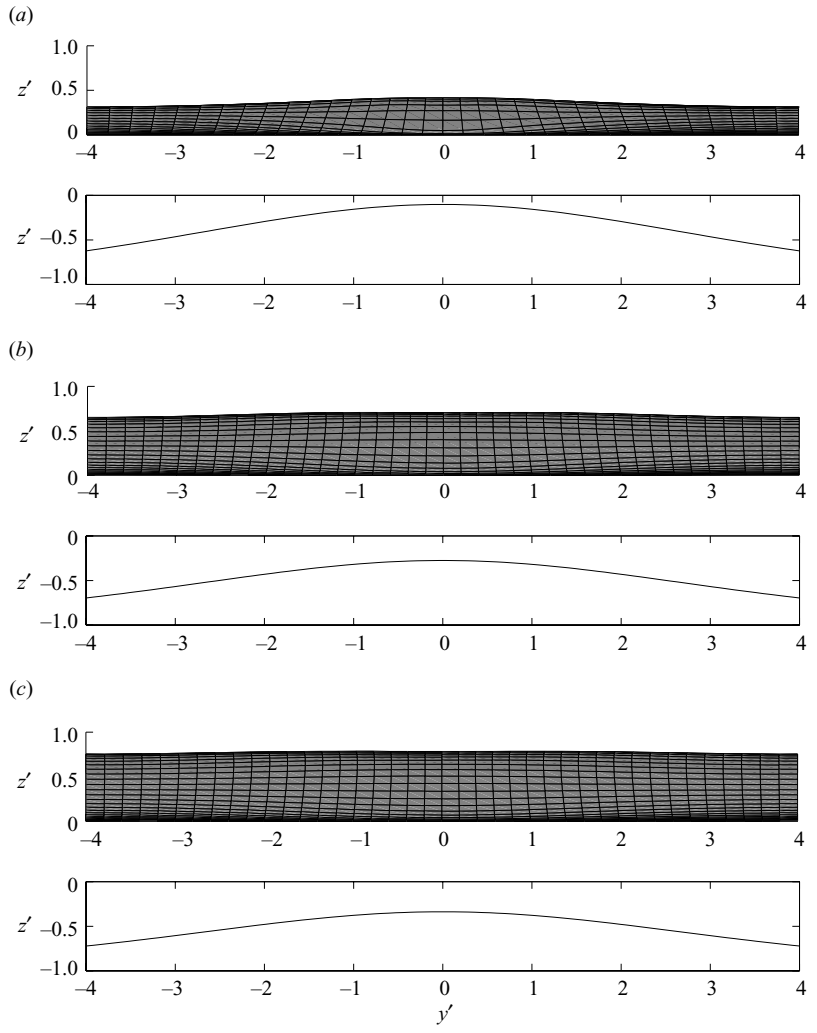

FIGURE 24. $k = 0.25$. Front view of wave (upper panel) and bottom (lower panel) profiles at the breaking point for (*a*) $H_0' = 0.3$ ($t_B' = 10.881$, $x_B' = 18.691$), (*b*) $H_0' = 0.6$ ($t_B' = 7.890$, $x_B' = 16.093$) and (*c*) $H_0' = 0.7$ ($t_B' = 7.250$, $x_B' = 15.164$).

Comparisons between two- and three-dimensional results for similar parameters have also been carried out. Overall, corresponding wave profiles at $y' = 0$ are found to be nearly identical, particularly near the plunging jet, but breaking occurs for slightly different times and x-locations in two and three dimensions. Everything else being equal, breaking takes more time to develop in the three-dimensional geometry than it does in the two-dimensional one. Moreover, our results for maximum particle velocity ($\sim 2c$) and acceleration (~ 5–$6g$) computed on the free surface are consistent with the two-dimensional results reported by New *et al.* (1985) and Dommermuth *et al.* (1988) for finite and infinite depth breakers, as well as with the three-dimensional results of Xue *et al.* (2001) for periodic breakers over infinite depth. Such similarities in near jet shape and dynamics of two- and three-dimensional plunging breakers seem to indicate that the flow near breaking jets, in the latest stages of wave overturning, becomes

almost independent of the background flow and boundary conditions (including bottom topography), that have induced breaking.

Although the present NWT is not capable of describing wave motion beyond the impact of the plunging jet on the free surface, it can be used to initialize accurately wave kinematics and pressure close to the breaking point in numerical models solving full NS equations (e.g. using volume of fluid (VOF) methods for the interface reconstruction and tracking). Usually, NS models are computationally very costly (particularly in three dimensions) and suffer from numerical diffusion, leading to artificial loss of energy over long distances of wave propagation. These can nevertheless realistically simulate the splash-up phenomenon, as reported in recent studies of two-dimensional breaking waves by Lin & Liu (1998) and Chen *et al.* (1999). Chen *et al.* (1999) performed direct simulations of NS equations, while Lin & Liu (1998) solved the Reynolds-averaged NS equations, together with a k–ϵ turbulent transport equation. A promising development seems to be the coupling of BEM and VOF methods for pre- and post-breaking waves, respectively, as done by Guignard *et al.* (1999) and Lachaume *et al.* (2003) in two dimensions, and Biausser *et al.* (2004) in three dimensions.

Finally, the use of a fast multipole algorithm to reduce the computational effort in the BEM has been proposed by Fochesato & Dias (2004) and applied to this NWT; this seems a promising way to make large-scale problems even more tractable.

We wish to thank the anonymous referees for their constructive comments and suggestions which have led to substantial improvements of the original manuscript. We thank in particular one of the referees for crucial insights on many physical aspects of the problem studied here. P. G. gratefully acknowledges financial support and disposal of computing resources from SHARCNET. S. T. G. acknowledges support from the US National Science Foundation, under grant CMS-0100223 of 'the Engineering/Earthquake, Hazards and Mitigation Program'.

REFERENCES

Baker, G. R., Meiron, D. I. & Orszag, S. A. 1982 Generalized vortex methods for free-surface flow problems. *J. Fluid Mech.* **123**, 477–501.

Banner, M. L. & Peregrine, D. H. 1993 Breaking waves in deep water. *Annu. Rev. Fluid Mech.* **25**, 373–397.

Biausser, B., Grilli, S. T., Fraunie, P. & Marcer, R. 2004 Numerical analysis of the internal kinematics and dynamics of 3D breaking waves on slopes. *Intl J. Offshore Polar Engng* **14**, 247–256.

Boo, S. Y., Kim, C. H. & Kim, M. H. 1994 A numerical wave tank for nonlinear irregular waves by three-dimensional higher-order boundary element method. *Intl J. Offshore Polar Engng* **4**, 265–272.

Brandini, C. & Grilli, S. T. 2001*a* Modelling of freak wave generation in a three-dimensional NWT. In *Proc. 11th Intl Offshore and Polar Engng Conf., Stavanger, Norway*, pp. 124–131. ISOPE.

Brandini, C. & Grilli, S. T. 2001*b* Three-dimensional wave focusing in fully nonlinear wave models. In *Proc. 4th Intl Symp. on Ocean Wave Measurement and Analysis, San Francisco, USA*, pp. 1102–1111. ASCE.

Broeze, J. 1993 Numerical modelling of nonlinear free surface waves with a three-dimensional panel method. PhD thesis, University of Twente, Enschede, The Netherlands.

Broeze, J., Van Daalen, E. F. G. & Zandbergen, P. J. 1993 A three-dimensional panel method for nonlinear free surface waves on vector computers. *Comput. Mech.* **13**, 12–28.

Celebi, M. S., Kim, M. H. & Beck, R. F. 1998 Fully nonlinear three-dimensional numerical wave tank simulations. *J. Ship Res.* **42**, 33–45.

Chang, K.-A. & Liu, P. L.-F. 1998 Velocity, acceleration and vorticity under a breaking wave. *Phys. Fluids* **10**, 327–329.

Chen, G., Kharif, C., Zaleski, S. & Li, J. 1999 Two-dimensional Navier–Stokes simulation of breaking waves. *Phys. Fluids* **11**, 121–133.

Clamond, D., Fructus, D., Grue, J. & Kristiansen, O. 2005 An efficient model for three-dimensional surface wave simulations. Part II: Generation and absorption. *J. Comput. Phys.* **205**, 686–705.

Cointe, R. 1990 Numerical simulation of a wave channel. *Engng Anal. Bound. Elem.* **7**, 167–177.

Dommermuth, D. G., Yue, D. K. P., Lin, W. M., Rapp, R. J., Chan, E. S. & Melville, W. K. 1988 Deep-water plunging breakers: a comparison between potential theory and experiments. *J. Fluid Mech.* **189**, 423–442.

Ferrant, P. 1996 Simulation of strongly nonlinear wave generation and wave–body interactions using a fully nonlinear MEL model. In *Proc. 21st Symp. on Naval Hydrodynamics, Trondheim, Norway*, pp. 93–108.

Fochesato, C. & Dias, F. 2004 Numerical model using the fast multipole algorithm for nonlinear three-dimensional free-surface waves. Submitted for publication.

Fochesato, C., Grilli, S. T. & Guyenne, P. 2005 Note on non-orthogonality of local curvilinear coordinates in a three-dimensional boundary element method. *Intl J. Numer. Meth. Fluids* **48**, 305–324.

Fructus, D., Clamond, D., Grue, J. & Kristiansen, O. 2005 An efficient model for three-dimensional surface wave simulations. Part I: Free space problems. *J. Comput. Phys.* **205**, 665–685.

Grilli, S. T., Guyenne, P. & Dias, F. 2001 A fully nonlinear model for three-dimensional overturning waves over an arbitrary bottom. *Intl J. Numer. Meth. Fluids* **35**, 829–867.

Grilli, S. T. & Horrillo, J. 1997 Numerical generation and absorption of fully nonlinear periodic waves. *J. Engng Mech.* **123**, 1060–1069.

Grilli, S. T. & Subramanya, R. 1994 Quasi-singular integrals in the modelling of nonlinear water waves in shallow water. *Engng Anal. Bound. Elem.* **13**, 181–191.

Grilli, S. T. & Subramanya, R. 1996 Numerical modelling of wave breaking induced by fixed or moving boundaries. *Comput. Mech.* **17**, 374–391.

Grilli, S. T., Subramanya, R., Svendsen, I. A. & Veeramony, J. 1994 Shoaling of solitary waves on plane beaches. *J. Waterway Port Coastal Ocean Engng* **120**, 609–628.

Grilli, S. T., Svendsen, I. A. & Subramanya, R. 1997 Breaking criterion and characteristics for solitary waves on slopes. *J. Waterway Port Coastal Ocean Engng* **123**, 102–112.

Grilli, S. T., Vogelmann, S. & Watts, P. 2002 Development of a three-dimensional numerical wave tank for modelling tsunami generation by underwater landslides. *Engng Anal. Bound. Elem.* **26**, 301–313.

Guignard, S., Grilli, S. T., Marcer, R. & Rey, V. 1999 Computation of shoaling and breaking waves in nearshore areas by the coupling of BEM and VOF methods. In *Proc. 9th Intl Offshore and Polar Engng Conf., Brest, France*, pp. 304–309, ISOPE.

Guyenne, P., Grilli, S. T. & Dias, F. 2000 Numerical modelling of fully nonlinear three-dimensional overturning waves over arbitrary bottom. In *Proc. 27th Intl Conf. on Coastal Engng, Sydney, Australia*, pp. 417–428.

Lachaume, C., Biausser, B., Grilli, S. T., Fraunie, P. & Guignard, S. 2003 Modeling of breaking and post-breaking waves on slopes by coupling of BEM and VOF methods. In *Proc. 13th Intl Offshore and Polar Engng Conf., Honolulu, USA,* pp. 353–359. ISOPE.

Lin, P. & Liu, P. L.-F. 1998 A numerical study of breaking waves in the surf zone. *J. Fluid Mech.* **359**, 239–264.

Longuet-Higgins, M. S. & Cokelet, E. D. 1976 The deformation of steep surface waves on water. I. A numerical method of computation. *Proc. R. Soc. Lond.* A **350**, 1–26.

Miles, J. W. 1977 Diffraction of solitary waves. *Z. Angew. Math. Phys.* **28**, 889–902.

New, A. L. 1983 A class of elliptical free-surface flows. *J. Fluid Mech.* **130**, 219–239.

New, A. L., McIver, P. & Peregrine, D. H. 1985 Computations of overturning waves. *J. Fluid Mech.* **150**, 233–251.

Pedersen, G. 1994 Nonlinear modulations of solitary waves. *J. Fluid Mech.* **267**, 83–108.

Peregrine, D. H. 1983 Breaking waves on beaches. *Annu. Rev. Fluid Mech.* **15**, 149–178.

Peregrine, D. H., Cokelet, E. D. & McIver, P. 1980 The fluid mechanics of waves approaching breaking. In *Proc. 17th Intl Conf. on Coastal Engng*, vol. **1**, pp. 512–528. ASCE.

Perlin, M., He, J. & Bernal, L. P. 1996 An experimental study of deep water plunging breakers. *Phys. Fluids* **8**, 2365–2374.

Skyner, D. J. 1996 A comparison of numerical predictions and experimental measurements of the internal kinematics of a deep-water plunging wave. *J. Fluid Mech.* **315**, 51–64.

Tanaka, M. 1986 The stability of solitary waves. *Phys. Fluids* **29**, 650–655.

Tong, R. P. 1997 A new approach to modelling an unsteady free surface in boundary integral methods with application to bubble–structure interactions. *Math. Comput. Simul.* **44**, 415–426.

Vinje, T. & Brevig, P. 1981 Numerical simulation of breaking waves. *Adv. Water Resources* **4**, 77–82.

Xü, H. & Yue, D. K. P. 1992 Computations of fully nonlinear three-dimensional water waves. In *Proc. 19th Symp. on Naval Hydrodynamics, Seoul, Korea.*

Xue, M., Xü, H., Liu, Y. & Yue, D. K. P. 2001 Computations of fully nonlinear three-dimensional wave–wave and wave–body interactions. Part 1. Dynamics of steep three-dimensional waves. *J. Fluid Mech.* **438**, 11–39.